




# Method for testing freeform surfaces based on a Shack-Hartmann sensor with plane wavefront scanning and stitching

JING WANG,<sup>1,2,3,4</sup> XIAOKUN WANG,<sup>1,2,3,4,6</sup> LIRONG PENG,<sup>1,3,4,5,7</sup>  
JINCHENG WANG,<sup>1,3,4</sup>  ZHONGKAI LIU,<sup>1,2,3,4</sup> LINGZHONG LI,<sup>1,2,3,4</sup>  
MENGXUE CAI,<sup>1,2,3,4</sup> BIN LIU,<sup>1,2,3,4</sup> WENHAN LI,<sup>1,2,3,4</sup>  
AND XUEJUN ZHANG<sup>1,2,3,4</sup>

<sup>1</sup>Changchun Institute of Optics, Fine Mechanics and Physics, Chinese Academy of Sciences, Changchun, Jilin 130033, China

<sup>2</sup>University of Chinese Academy of Sciences, Beijing 100049, China

<sup>3</sup>Key Laboratory of Optical System Advanced Manufacturing Technology, Chinese Academy of Sciences, Changchun, Jilin 130033, China

<sup>4</sup>State Key Laboratory of Applied Optics, Changchun, Jilin 130033, China

<sup>5</sup>School of Mechanical and Aerospace Engineering, Jilin University, Changchun, Jilin 130025, China

<sup>6</sup>jimwxk@sohu.com

<sup>7</sup>penglirong@ciomp.ac.cn

**Abstract:** Currently, the surface error measurement technology for freeform faces a significant contradiction between measurement accuracy and dynamic range. The study proposes a non-null testing method for measuring freeform surfaces by utilizing a Shack-Hartmann wavefront sensor to emit a small aperture parallel beam and scan along the normal direction at the center of subapertures for stitching (SHPSS). A mathematical model based on ray tracing and the reflection theorem is established to calculate the sampling points on an ideal freeform surface, the reference spot array on CCD, and the corresponding relationship between microlens array and spots. An algorithm is proposed to iteratively calculate the wavefront aberration and gradually approach the actual sampling points using the established model. Theoretical analysis and numerical simulation results indicate that SHPSS can increase the dynamic range and improve the accuracy of wavefront reconstruction. The error analysis of the SHPSS method is carried out, the measurement accuracy of full aperture freeform surface is 11.45 nm. A testing system is set up and experiments are conducted on a 100 mm aperture freeform reflective mirror. The RMS of the SHPSS test results is less than  $\lambda/30$  ( $\lambda=635$  nm) compared to the interferometric test results. By analyzing five groups of repeated measurement experiments, the repeatability accuracy of SHPSS method is less than  $1/80 \lambda$  (RMS). This demonstrates the feasibility and measurement capabilities of the method for freeform surface testing.

© 2023 Optica Publishing Group under the terms of the [Optica Open Access Publishing Agreement](#)

## 1. Introduction

Optical freeform surfaces primarily refer to non-rotationally symmetric surfaces. Compared to spherical surfaces, non-spherical surfaces offer greater design freedom to manipulate surface shapes. While meeting the high performance, lightweight and miniaturization requirements of modern optical systems, they can be utilized to provide targeted correction of aberrations along and off-axis. They hold significant potential for extensive applications in fields such as illumination, display, and imaging [1,2]. However, the high precision requirements for optical element surface shapes in the imaging field limit the large-scale application of freeform surfaces [3,4]. Especially, the measurement technology of freeform surfaces has become the most critical factor restricting their application. In particular, the test of freeform surfaces mainly faces a contradiction between

measurement accuracy and dynamic range of curvature [5,6]. High-precision surface metrology is typically accomplished using interferometers. The method of computational holography not only requires customized computer-generated holograms (CGH) specific to the testing element but also faces limitations in the design and fabrication of CGH when testing freeform surfaces [7]. Furthermore, interferometry requires strict control of experimental conditions such as vibrations and temperature [8]. Subaperture stitching techniques have been widely applied in optical freeform surface error measurements [9]. The non-null testing technology has more flexibility for the measurement of freeform surfaces [10–12]. Shack-Hartmann technology is not only insensitive to vibrations but also has a large dynamic measurement range. It allows high-precision surface error measurement without the need for a reference wavefront. It's flexible and excellent choice for freeform surface testing [13,14].

In 2008, Florit et al. utilized a high-precision Shack-Hartmann wavefront sensor (SHS) as a measurement head mounted on a translation stage to meet the requirements of short-wavelength optical X-ray reflection mirror surface error measurement. By performing two-dimensional translation measurements and stitching subapertures, the system achieved sub-micrometer sensitivity and a large dynamic range for high-curvature surfaces. It could measure the minimum curvature radius of 879 mm [15]. In 2014, Mourad et al. proposed a two-dimensional slope measurement system based on a stitched Hartmann optical head. The system was designed for high-precision optical measurements of X-ray reflection mirrors. The slope error accuracy achieved was better than RMS 50 nrad [16]. In 2015, Kamal et al. proposed a method for measuring the wavefront of PMMA freeform surfaces using a scanning SHS and subaperture stitching technique. The method involved active numerical alignment to minimize lateral errors and further corrected vertical position errors using a least-squares fitting approach [17]. In 2017, Dali et al. proposed a scheme for the non-null measurement of transmissive wavefronts of freeform surfaces using subaperture stitching. They also established a library of residual slope errors to minimize misalignment errors during the scanning process. This technique could test the surface error of freeform with manufacturing precision within one wavelength ( $0.63\ \mu\text{m}$ ) [18]. In 2017, Dali utilized a scanning SHS to develop an experimental setup for measuring reflective surfaces. They used the setup to measure a Stavax ESR (alloy steel) freeform mirror [19]. In 2020, Oliver et al. proposed an extension to the Hartmann testing capability by introducing a wavefront deformation vector equation. They used the method to measure the high-order aberration wavefront of a progressive addition lens (PAL) after refraction, with a relative error of 1.93% [20]. At present, the measurements combining Shack-Hartmann method and sub-aperture stitching technique predominantly employ two-dimensional stitching. Although these methods have high accuracy in measuring the slope error of the X-ray mirror, when applied to the freeform surface test with a small curvature radius, the deviation of the detected spot increases, beyond the dynamic range, resulting in the measurement accuracy is limited, and some of the reflected light may not return to the sensor, and the test cannot be completed.

Therefore, a method for testing the surface error of freeform using a Shack-Hartmann wavefront sensor based on plane wavefront scanning and stitching is proposed. Unlike the conventional Shack-Hartmann method that utilizes a spherical wavefront as a reference to measure freeform surfaces, the method proposed is a non-null measurement scheme that does not require a reference wavefront. By using a planar wavefront as the incident light, the mathematical model based on ray tracing is simplified, reducing the complexity and difficulty of computing the reference spot array. The advantage of the plane wave incident along the normal direction of the subaperture on the freeform surface is that it increases the dynamic measurement range. Utilizing an iterative algorithm to compute the actual sampling points on the freeform surface can improve the accuracy of wavefront reconstruction. Additionally, the method of small-aperture stitching increases the sampling rate, which can improve the measurement resolution.

The study presents the scanning and stitching method based on the SHS and its principles. The equation for calculating the reference sampling points on an ideal freeform surface is derived by utilizing the precise relationship between the incident light and the reflected light in the reflection theorem. The algorithmic process for approximating the actual measurement points on a freeform surface using an iterative method is described. For the situation where sub-aperture measurements are conducted along the normal direction of freeform surfaces, a method is presented to compute the reference spot using theoretical models and directly calculate the surface slope of the freeform surface. Theoretical analysis is conducted to determine the applicable conditions and dynamic range of this method. Numerical simulations are performed using a theoretical model, and the results demonstrate the feasibility of this method. In addition, a numerical simulation iterative algorithm is used to reconstruct surface errors of different sizes, and the results show that the iterative method can improve the accuracy of wavefront reconstruction. A system is constructed and successfully implements for the measurement of freeform reflective mirror. Experimental measurement results are provided, along with a comparison to results obtained from interferometric measurement. This comparison validated the effectiveness of the SHPSS method for freeform surface error measurement.

## 2. Theory of SHPSS

SHPSS utilizes the SHS to emit a small-caliber collimated beam of parallel light and scan it along the normal direction of the sub-aperture center. The obtained subaperture slope data is reconstructed and stitched through wavefront reconstruction to obtain the full aperture surface error. The optical path of SHPSS is illustrated in Fig. 1. The spherical wave generated by a laser point source is collimated by a collimator lens to form parallel light. The parallel light is reflected by a beam splitter, deflecting it by  $90^\circ$ . It then vertically illuminates the aperture region of the tested freeform mirror, carrying surface error information. The reflected light containing the surface error information passes through the beam splitter and is spatially sampled by a microlens array according to its arrangement, dividing it into small beams. The converging spot images of these small beams are formed on a CCD detector located at the focal plane of the microlens array. To minimize the displacement of the spot and maximize the amount of reflected light returning to the detector, it is necessary to adjust the position and orientation of the SHS to ensure that the parallel light is incident along the normal direction of the sub-aperture center. According to the subaperture planning, the sensor is deflected to achieve the translation and rotation of the tested mirror, completing a full aperture scanning test.

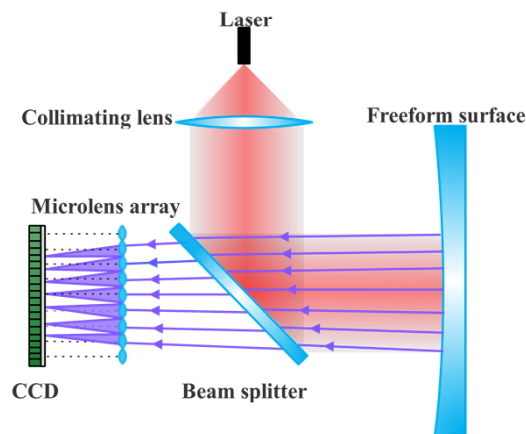


**Fig. 1.** Optical path diagram of SHPSS method.

The SHS tests the wavefront incident on the micro-lens array. Due to the propagation of the wavefront, there is a discrepancy between the coordinate systems of the micro-lens array and the initial wavefront. As a result, the tested wavefront slopes on the micro-lens array cannot accurately correspond to their positions on the initial wavefront. Typically, an approximation using the centroid coordinates of the micro-lens array is employed, leading to the introduction of low-order aberrations during wavefront reconstruction. By utilizing ray tracing and iterative methods to compute the actual coordinate of the sampled points on the mirror surface and the slope of the reconstructed wavefront, the accuracy of wavefront reconstruction can be improved.

The expression of freeform surface profiles varies depending on the specific requirements. In simulation and experimental studies, the representation of freeform surface profiles is commonly described as follows:

$$Z(X, Y) = -\frac{\frac{X^2}{R_x} + \frac{Y^2}{R_y}}{1 + \sqrt{1 - (1 + k_x) \cdot \frac{X^2}{R_x^2} + (1 + k_y) \cdot \frac{Y^2}{R_y^2}}} + \sum_{i=1}^n C_i Z_i(x, y) \quad (1)$$

In this case,  $k_x$  and  $k_y$  represent the conic coefficients in the x and y directions respectively,  $Z_i$  is the standard Zernike polynomial in Cartesian coordinates,  $C_i$  denotes the coefficients of each term,  $R_x$  and  $R_y$  are the vertex curvature radii in the x and y directions respectively, and  $x = X/R$ ,  $y = Y/R$ , where R represents the semi-aperture of the freeform reflective surface.

The subaperture planning for a full aperture coverage should start from the center of the freeform reflective mirror, denoted as point O. This center point O also serves as the center for the subapertures, which are circular in shape with a diameter of D (the aperture of the SHS for the outgoing parallel beam). In the yoz plane, through the free-form surface expression  $F(x, y, z) = 0$ , the curve equation can be obtained as  $F(0, y, z) = 0$ , denoted as  $G(y, z) = 0$ . In order to achieve full aperture coverage, adjacent subapertures need overlapping areas. The spatial distance from the start of the m-th ring to the start of the (m-1)-th ring is D/2. The starting point  $S_{m-1}(0, y_{m-1}, z_{m-1})$  of the m-th circle is obtained by solving the Eq. (2).

$$\begin{cases} G(y, z) = 0 \\ |S_{m-1} S_{m-1}| = \sqrt{(y_{m-1} - y_{m-1-1})^2 + (z_{m-1} - z_{m-1-1})^2} = \frac{D}{2} \end{cases} \quad (y > 0) \quad (2)$$

The spacing between adjacent sub-apertures in the m-th ring is also D/2. The center point of the nm-th sub-aperture  $S_{m\_nm}(x_{m\_nm}, y_{m\_nm}, z_{m\_1})$  in the m-th circle is obtained by solving the Eq. (3).

$$\begin{cases} F(x, y, z_{m-1}) = 0 \\ |S_{m\_nm-1} S_{m\_n2}| = \sqrt{(x - x_{m\_nm-1})^2 + (y - y_{m\_nm-1})^2} = \frac{D}{2} \end{cases} \quad (3)$$

The nm is the number of subapertures in the m-th ring. The number of subapertures is required in the Eq. (4).

$$|S_{m-1} S_{m\_nm}| < \frac{D}{2} \quad (4)$$

By calculate the center positions (x, y, z) of the subapertures, the normal direction of the subaperture is calculated by using the partial derivative. The sub-aperture layout results are shown in Fig. 2.

According to the subaperture layout results, for the central subaperture, parallel light enters along the direction of the optical axis (parallel to the normal direction of the central sub-aperture), as shown in Fig. 3(a). For the non-central subapertures, parallel light enters along the normal direction of their sub-aperture centers respectively, as shown in Fig. 3(b). The freeform surface refers to an actual reflective mirror with surface errors. Parallel light **I** is incident on the freeform

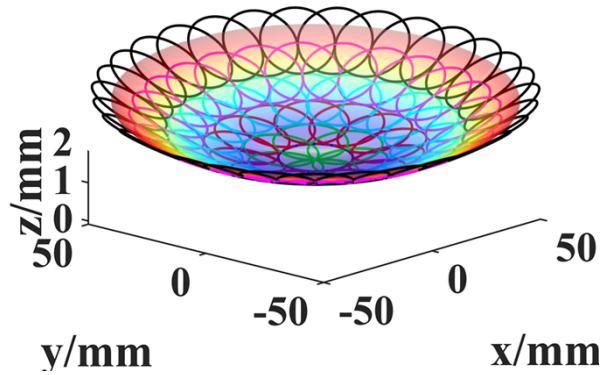


Fig. 2. Subaperture planning result.

surface mirror at the point  $P(x, y, z)$ . The freeform surface normal direction at point P is denoted as  $\mathbf{N}$ . The reflected ray  $\mathbf{R}$  passes through the center  $P_0(x_0, y_0, z_0)$  of a microlens and intersects with the plane where the CCD is located at the point  $P_1(x_1, y_1, z_1)$ . The extended line of the reflected ray intersects with the ideal freeform surface at the point  $P_2(x_2, y_2, z_2)$ . Assume the microlens is an ideal thin lens and has a sufficiently small aperture, the intersection point between the principal ray and the CCD can be considered as the centroid of the optical spot. In this context,  $b$  represents the distance between the microlens array and the subaperture center, and  $f$  represents the focal length of the microlens. The distance between the microlens and the CCD is also equal to  $f$ . The dashed lines represent the reference optical path of an ideal freeform reflective mirror.

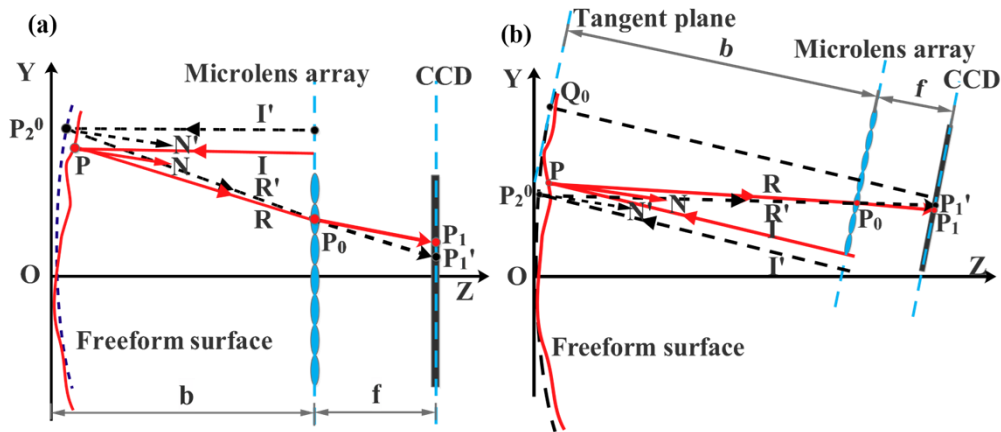


Fig. 3. Ray tracing diagram for testing actual freeform surface. (a) Ray tracing diagram for testing central subaperture, (b) Ray tracing diagram for testing non-central subaperture.

The expression for the freeform surface profile can also be written using Eq. (1).

$$F(x, y, z) = f(x, y) - Z = 0 \tag{5}$$

$Z$  is the height of the free-form surface.  $f(x, y)$  is the expression of free-form surface.

The unit normal vector  $\mathbf{N}(N_x, N_y, N_z)$ , at point P on the mirror surface can be obtained by analyzing the data collected from the SHS. The specific calculation process is described in section 3.2.

The reflection light ray passes through the point  $P_2(x_2, y_2, z_2)$  and the center point of the micro-lens. The unit direction vector  $\mathbf{R}$  of the reflected light ray is determined by the following equation:

$$\mathbf{R}(R_x, R_y, R_z) = P_0 - P_2 = \frac{(x_0 - x_2, y_0 - y_2, z_0 - z_2)}{\sqrt{(x_0 - x_2)^2 + (y_0 - y_2)^2 + (z_0 - z_2)^2}} \quad (6)$$

For the central subaperture, the unit direction vector  $\mathbf{I}$  of the incident light is parallel to the normal direction of the subaperture center.

$$\mathbf{I}(I_x, I_y, I_z) = (0, 0, -1) \quad (7)$$

For a non-central subaperture with the center point  $Q_0$ , the unit direction vector of the incident light  $\mathbf{I}$  is:

$$\mathbf{I}(I_x, I_y, I_z) = \frac{(f_x, f_y, -1)}{\sqrt{f_x^2 + f_y^2 + 1}} |Q_0(x, y, z) \quad (8)$$

According to the reflection theorem,

$$\mathbf{R} = \mathbf{I} - 2 \times (\mathbf{I} \cdot \mathbf{N})\mathbf{N} \quad (9)$$

From the above equation,

$$\mathbf{N} = \frac{\mathbf{R} - \mathbf{I}}{|\mathbf{R} - \mathbf{I}|} \quad (10)$$

$$\frac{N_x}{N_z} = \frac{R_x - I_x}{R_z - I_z}, \frac{N_y}{N_z} = \frac{R_y - I_y}{R_z - I_z} \quad (11)$$

By combining Eqs. (5) and (10) simultaneously, the intersection point  $P_2(x_2, y_2, z_2)$  of the reflected ray passing through the center of the microlens and the ideal freeform surface can be solved.

$$\begin{cases} x_0 - x_2 + \frac{N_x}{N_z} \cdot (z_0 - z_2) - \left(I_x + \frac{N_x}{N_z} \cdot I_z\right) \cdot \sqrt{(x_0 - x_2)^2 + (y_0 - y_2)^2 + (z_0 - z_2)^2} = 0 \\ y_0 - y_2 + \frac{N_y}{N_z} \cdot (z_0 - z_2) - \left(I_y + \frac{N_y}{N_z} \cdot I_z\right) \cdot \sqrt{(x_0 - x_2)^2 + (y_0 - y_2)^2 + (z_0 - z_2)^2} = 0 \\ f(x_2, y_2) - z_2 = 0 \end{cases} \quad (12)$$

To achieve an ideal wavefront reconstruction, two pieces of data are required. One is the accurate wavefront slope data, and the other is the precise coordinate positions of the sampling points on the original wavefront associated with the slopes [21]. However, the surface error of a freeform surface can lead to deviations in the propagated wavefront. The accurate positions of the wavefront slope sampling points cannot be directly determined, so it is necessary to find an approximate point and substitute its coordinates into the reconstruction algorithm. In the traditional Shack-Hartmann method, the center of the microlens array is commonly used as an approximate point for wavefront slope sampling in wavefront reconstruction. However, this coordinate approximation leads to errors in the reconstructed wavefront [22]. As shown in Fig. 3, due to the normal direction along the center of the subaperture, the coordinate system of the sensor is different from the original wavefront coordinate system. Therefore, it is not possible to substitute the center of the microlens array for the sampled points of the wavefront slope. The reference sampling point  $P_2^0$  on the ideal freeform surface can be used as an approximate point. However, the coordinate deviation between it and the actual sampling point P still affects the accuracy of wavefront reconstruction.

Therefore, an iterative method is proposed to make the approximate point closer to the actual sampling point P, thereby improving the accuracy of wavefront reconstruction. The iteration

count is denoted by the superscript  $l$ . In the  $l$ -th iteration, the coordinates of the refined point  $P_2$  are represented as  $P_2^l(x_2^l, y_2^l, z_2^l)$ . First, the sampling point  $P_2^0$  on the ideal freeform surface obtained from the model calculation is used as the initial approximate point. The point  $P_2^0(x_2^0, y_2^0, z_2^0)$  is substituted into the wavefront reconstruction algorithm, and the least squares method is used to solve [23] and fit the full aperture surface error  $W^l$ . The surface error  $W^l$  is mathematically analytically fitted using the Zernike polynomial expression of the first 36 terms.

$$W^l = \sum_1^{i=36} C_i Z_i(x_2^{l-1}, y_2^{l-1}, z_2^{l-1}) \quad (13)$$

Based on the given notations, where  $Z_i$  represents the Zernike polynomials and  $C_i$  represents the corresponding coefficients of each term.

Therefore, the new freeform surface profile can be expressed as:

$$\Sigma^l = \Sigma^0(x_2^{l-1}, y_2^{l-1}, z_2^{l-1}) + W^l \quad (14)$$

where the ideal freeform surface profile  $\Sigma^0$  is expressed by Eq. (1).

The sampling points  $P_2^l$  on the new reference surface  $\Sigma^l$  are recalculated using Eq. (12) with  $\Sigma^l$  being utilized as the new freeform reference surface.

$$\begin{cases} x_0 - x_2^l + \frac{N_x}{N_z} \cdot (z_0 - z_2^l) - \left( I_x + \frac{N_x}{N_z} \cdot I_z \right) \cdot \sqrt{(x_0 - x_2^l)^2 + (y_0 - y_2^l)^2 + (z_0 - z_2^l)^2} = 0 \\ y_0 - y_2^l + \frac{N_y}{N_z} \cdot (z_0 - z_2^l) - \left( I_y + \frac{N_y}{N_z} \cdot I_z \right) \cdot \sqrt{(x_0 - x_2^l)^2 + (y_0 - y_2^l)^2 + (z_0 - z_2^l)^2} = 0 \\ \Sigma^0(x_2^{l-1}, y_2^{l-1}, z_2^{l-1}) + W^l - z_2^l = 0 \end{cases} \quad (15)$$

By iteratively refining the freeform surface error to better approximate the real situation, it is possible to obtain approximate points that are closer to the actual sampled points. Repeat the above steps until the reconstructed surface error approaches convergence, which means that the root mean square (RMS) of the absolute difference between the two fitted surface errors is sufficiently small. In our research, the value is  $\lambda/100$  ( $\lambda=635$  nm). The evaluation criterion for surface convergence is determined by

$$|RMS(W^l) - RMS(W^{l-1})| < \lambda/100 \quad (16)$$

### 3. SHPSS calculation method

#### 3.1. Calculate the reference spot of freeform

The main challenge in measuring the surface error of freeform surfaces using the Shack-Hartmann method lies in the significant curvature variations of the freeform surface, which may exceed the dynamic range of the SHS. This confuses the correspondence between the spots and micro-lenses, leading to errors in the calculation of surface slope [24]. Furthermore, the irregularity of the spots in relation to the test point makes it impossible to utilize traditional grid averaging methods for centroid calculation [25]. By employing a parallel light normal incident aperture, it is possible to reduce the deviation of the spot and simplify the calculation of ray tracing for the spot reference point during relative detection, thereby decreasing the computational complexity.

Using a collimated light to measure freeform surfaces can introduce system errors. Therefore, it is beneficial to establish a numerical simulation model by tracing rays on an ideal surface shape of the freeform surface, as shown in Fig. 4. By calculating the spot positions as a reference file during relative measurements, this approach can help eliminate system errors.

Indeed, in the construction of SHS, there is a strict parallel position relationship between the outgoing plane wave and the micro-lens array surface as well as the CCD plane. This parallel

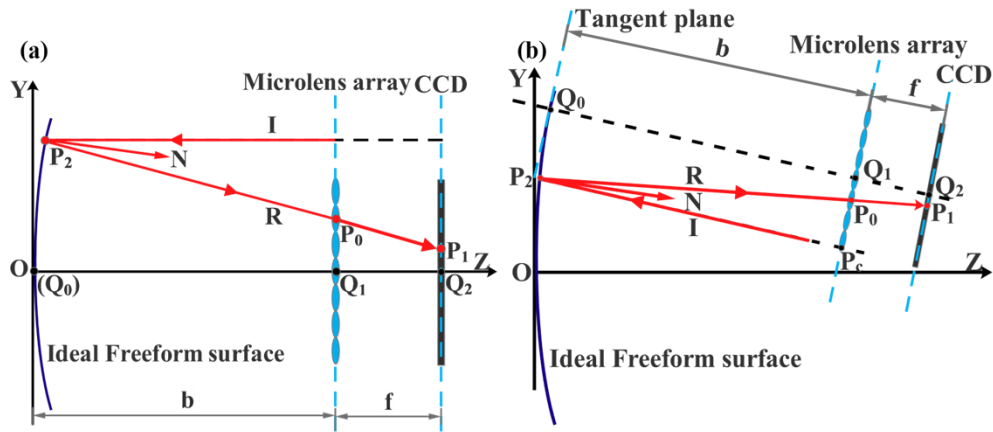


**Fig. 4.** Ray tracing diagram for testing ideal freeform surface. (a) Ray tracing diagram for testing central subaperture, (b) Ray tracing diagram for testing non-central subaperture.

configuration is crucial for maintaining the accuracy of the measurements. Therefore, the centroid matrix of the micro-lens array in the SHS after adjusting its position can be calculated using the Rodriguez rotation matrix.

The initial normal vector of the micro-lens array surface is given by  $\mathbf{I}_0(0, 0, -1)$ , along the direction of the optical axis. After adjusting the SHS the normal vector of the micro-lens array surface becomes aligned with the incident parallel light and is represented as  $\mathbf{I}(I_x, I_y, I_z)$ , as shown in Eq. (8). The plane determined by  $\mathbf{I}$  and  $\mathbf{I}_0$  necessarily has a normal vector which corresponds to the rotation axis (Note: the rotation axis is not necessarily the normal vector of the plane itself). The normal vector can be obtained by taking the cross product of the two vectors. Based on the aforementioned information, the unit vector of the rotation axis can be denoted as  $\mathbf{n}(n_x, n_y, n_z)$ .

$$\mathbf{n}(n_x, n_y, n_z) = \mathbf{I}_0 \times \mathbf{I} = (I_y, -I_x, 0) \quad (17)$$

The rotation angle between two vectors can be obtained through dot product.

$$\theta = \arccos \frac{\mathbf{I}_0 \cdot \mathbf{I}}{|\mathbf{I}_0| |\mathbf{I}|} = \arccos \frac{1}{\sqrt{f_x^2 + f_y^2 + 1}} |Q_0(x, y, z)| \quad (18)$$

The calculated Rodrigues rotation matrix is denoted as L.

$$\begin{pmatrix} \cos\theta + I_y^2(1 - \cos\theta) & -I_x I_y(1 - \cos\theta) & -I_x \sin\theta \\ -I_x I_y(1 - \cos\theta) & \cos\theta + I_x^2(1 - \cos\theta) & -I_y \sin\theta \\ I_x \sin\theta & I_y \sin\theta & \cos\theta \end{pmatrix} \quad (19)$$

According to the results of subaperture planning, let  $Q_0$  represent the center point of the subaperture,  $Q_1$  the center point of the plane where the microlens array is located, and  $Q_2$  the center point of the plane where the CCD is located. The three points  $Q_0$ ,  $Q_1$  and  $Q_2$ , are collinear. The direction of the line is defined as the direction of incident parallel light, denoted as  $\mathbf{I}(I_x, I_y, I_z)$ . The distance between  $Q_0$  and  $Q_1$  is denoted as  $b$ , and the distance between  $Q_1$  and  $Q_2$  is denoted as  $f$ . The reflected ray  $\mathbf{R}$  travels from point  $P_2$  on the freeform surface, passes through the center  $P_0$  of the microlens, and intersects with the CCD at point  $P_1$ . Therefore, the reference spot is sought, which means finding the test point between the reflected ray  $\mathbf{R}$  and the plane



where the CCD is located. In Section 2, by employing ray tracing and the law of reflection, the coordinates of the actual sampling points  $P_2(x_2, y_2, z_2)$  on the freeform surface and the center point  $P_0(x_0, y_0, z_0)$  that the reflected light passes through are calculated. Thus, the equation of the straight line on which the reflected ray lies can be expressed as:

$$\frac{x - x_0}{x_0 - x_2} = \frac{y - y_0}{y_0 - y_2} = \frac{z - z_0}{z_0 - z_2} \quad (20)$$

The Eq. (18) represents the space position of the CCD plane.

$$I_x(x - x_{Q_0}) + I_y(y - y_{Q_0}) + I_z(z - z_{Q_0}) = 0 \quad (21)$$

By utilizing Eqs. (16) and (17), it is possible to determine the coordinates of the reference spot. For freeform surfaces, the reference spot is not a regular rectangular grid, and the correspondence between the spot and the microlens cannot be considered based on the nearest principle. By tracing the rays passing through the center of the microlens and intersecting with the CCD, the position of the reference spot can be calculated for the ideal freeform surface. This enables the establishment of the correspondence between the reference spot and the microlens array. Simultaneously, for the irregular spot patterns on the CCD during actual test, the position of the reference spot can be used to search for the centroid of the actual spot nearby. This approach avoids the problem of incorrect centroid identification caused by traditional grid segmentation. Once the centroid of the actual spot is determined, it should be placed at the corresponding matrix position of the microlens array.

The measurement sensitivity of SHS is mainly determined by the pixel size of the CCD. Typically, the measurement accuracy of the spot centroid in SHS has reached a precision of 1/2000 of a pixel unit. Therefore, the sensitivity  $\theta_{min}$  of the sensor is given by [26,27]:

$$\theta_{min} = \frac{P}{2000f} \quad (22)$$

P represents the unit pixel length, and f represents the focal length of the microlens. Based on the information provided, the measurement sensitivity of the SHS is 0.89  $\mu\text{rad}$ , with a CCD pixel size of 7.3  $\mu\text{m}$  and a microlens focal length of 4.1 mm.

### 3.2. Calculate the slope of freeform directly

The traditional Shack-Hartmann method utilizes the positional displacement of the tested spots relative to the reference spots to calculate the average slope of the wavefront aberration between the measured wavefront and the reference wavefront [28]. Due to the method proposed, the reference planes of each subaperture are different, which makes it impossible to unify them on the same plane. Based on the characteristic of the method, which involves knowing the direction vector of the incident light rays, it is possible to calculate the direction vector of the reflected light rays based on the Shack-Hartmann measurement results. Therefore, a method is proposed to directly calculate the slope of the freeform surface by using the reflection theorem and the similarity relationship of triangles. By utilizing the disparity between the computed slope and the ideal slope of the freeform surface at the corresponding sampling points as the mean slope of the surface error, it is possible to reduce the impact of coordinate positioning errors and slope errors on the accuracy of wavefront reconstruction.

Figure 5 illustrates the relationship between the displacement of a single micro-lens spot and the slope of the freeform surface. The distance between the micro-lens array and CCD is f, and it is perpendicular to the incident parallel light **I** (the normal vector at the center of the sub-aperture). The reflected ray **R** passes through the center  $P_0$  of the micro-lens and intersects the CCD at point  $P_1$ .  $P_t$  is the projection of  $P_0$  onto the CCD plane along the incident direction. Based on

the principle of SHS, the relationship of the light spot deviation depicted in the Fig. 5 is as the reflection relationship of a freeform surface, i.e.,  $\Delta P_0 P_1 P_t$  is similar to  $\Delta P_2 P_0 P_c$ . Hence, the normal vector obtained from an individual micro-lens calculation represents the normal vector of the test point  $P_2$  on the freeform surface.

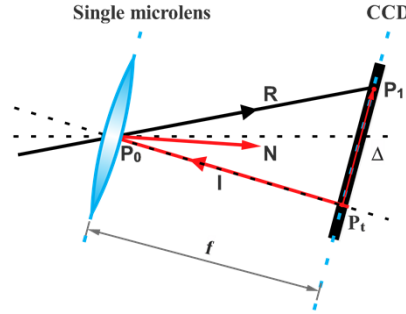


**Fig. 5.** Schematic diagram illustrating the relationship between the displacement of a single microlens spot and the slope of the freeform surface.

The SHS can obtain the deviation of the light spot within the CCD plane as  $(\Delta x, \Delta y)$ . In our research, the displacement of the light spot is a three-dimensional vector  $\Delta(\Delta x, \Delta y, \Delta z)$  due to the pose variation of the SHS. By considering the perpendicular relationship between the incident ray  $\mathbf{I}$  and the CCD plane, it is possible to calculate  $\Delta z$ .

$$\Delta z = -\frac{I_x \cdot \Delta x + I_y \cdot \Delta y}{I_z} \quad (23)$$

$\mathbf{R}$  represents the reflected ray.

$$\mathbf{R} = \Delta - \mathbf{I} = \frac{(\Delta x - f \cdot \Delta I_x, \Delta y - f \cdot \Delta I_y, \Delta z - f \cdot \Delta I_z)}{\sqrt{(\Delta x - f \cdot \Delta I_x)^2 + (\Delta y - f \cdot \Delta I_y)^2 + (\Delta z - f \cdot \Delta I_z)^2}} \quad (24)$$

According to the law of reflection, the normal vector  $\mathbf{N}$  of the freeform surface can be obtained, which represents the partial derivatives of the freeform surface along various directions and the slopes of the freeform surface along the  $x$  and  $y$  directions.

$$\begin{cases} Z_x = N_x = \frac{I_x - R_x}{R_z - I_z} \\ Z_y = N_y = \frac{I_y - R_y}{R_z - I_z} \\ Z_z = N_z = -1 \end{cases} \quad (25)$$

By substituting the ideal freeform surface into the model, it is possible to calculate the slope of the sampling point  $P_2^0$  on the ideal freeform surface, which represents the initial reference slope. The reference slopes can indeed vary for different sampling points. Therefore, the new reference slopes are obtained by iteratively computing the slopes of the new sampling point on the ideal freeform surface. Due to the adoption of the subaperture parallel light normal incidence testing method, the reference surfaces of each subaperture are planes with different spatial positions and slopes. In other words, the reference surfaces of each sub-aperture are different and cannot be stitched together into a smooth reference surface. Therefore, the surface error  $W^1$  is obtained by performing a least squares fitting on the full aperture information using the difference between the actual slopes and the reference slopes. Subsequently, the wavefront is reconstructed using the iterative method described in Section 2.

Due to the adoption of a plane wavefront incident, the beam undergoing reflection on the freeform surface will experience diffraction or convergence. When the freeform surface is convex, if the aperture diameter of the reflected subaperture beam exceeds twice the diameter of the CCD, the resulting tested area is significantly reduced. When the freeform surface is concave, if the aperture diameter of the reflected subaperture beam is smaller than half the diameter of the CCD, the number of spots decreases, resulting in a reduced sampling rate. For convex freeform surfaces, it is necessary for the slope at the edge of the subaperture, denoted as  $Slope_{edge}$  to satisfy a specific relationship with the slope at the center of the subaperture, denoted as  $Slope_{center}$ .

$$|Slope_{edge} - Slope_{center}| < \frac{L}{2b} \quad (26)$$

For concave freeform surfaces,

$$|Slope_{edge} - Slope_{center}| < \frac{L}{4b} \quad (27)$$

The CCD size is  $L \times L$ , and  $b$  represents the measuring distance, which is the distance from the center of the subaperture to the microlens array. In the study, the CCD size is 14.6 mm  $\times$  14.6 mm, and the measuring distance is 10 mm. For concave freeform surfaces, the absolute difference between  $Slope_{edge}$  and  $Slope_{center}$  must be less than 0.365 rad.

The traditional dynamic range  $\theta_{max}$  is primarily determined by the aperture and focal length of the microlens [26,27].

$$\theta_{max} = \frac{D}{2f} - 1.22 \frac{\lambda}{D} \quad (28)$$

$D$  corresponds to the aperture of the microlens, while  $\lambda$  represents the wavelength. The microlens aperture used in the SHS is  $D = 0.114$  mm, with a wavelength of  $\lambda = 635$  nm. The traditional dynamic range is measured to be 7.1 mrad.

Expanding the dynamic range of a SHS primarily involves aligning the deviations of the light spots with the reference light spot. The test results of the SHS exhibit a smoothing effect on mid-to-high-frequency information. Consequently, the entropy contribution from the light spot deviation for mid-to-high-frequency information is minimal, with its main impact being on low order aberrations. When the low order aberrations are smaller than the system aberrations of a plane wavefront incident on a freeform surface, the light spot deviation occurs in the vicinity of the reference light spot, and there is no cross-interference among adjacent light spots. Therefore, when testing distances of 10 mm, the dynamic range is expanded from 7.1 mrad to a maximum of 0.365 rad, which is 50 times larger compared to the traditional dynamic range.

## 4. Numerical simulation and precision analysis

### 4.1. System model simulation results

In this section, numerical simulation is used to verify the feasibility of the proposed method and demonstrate the advantages of the iterative approach. The simulation results presented below are subject to limitations imposed by the computational precision. Non-rotationally symmetric freeform surfaces can be represented using a linear combination of Eq. (1), where  $R_x = 255.98$  mm,  $R_y = 253.38$  mm,  $k_x = -0.977$ ,  $k_y = -0.978$ . By selecting the first nine terms of the Zernike polynomials, the coefficients  $C_i$  are sequentially chosen as follows: (-0.205,  $4.609 \times 10^{-4}$ , 0.114, -0.205,  $-4.828 \times 10^{-5}$ , 0.0679,  $6.743 \times 10^{-3}$ ,  $1.191 \times 10^{-5}$ ,  $-2.872 \times 10^{-5}$ ). The Fig. 2 represents the surface profile map of the non-rotationally symmetric freeform surface.

Firstly, selecting a measuring distance of  $d = 10$  mm, the spatial positions and angular orientations during normal incidence are calculated for each individual subaperture, while ensuring complete coverage of the entire aperture. Subsequently, simulations are performed

based on the mathematical model established in Section 2, illustrating the test optical paths as depicted in Fig. 6(a), 6(b), and 6(c). The simulation results for the central subaperture, the second concentric subaperture, and the third concentric subaperture are listed as follows. Using the method proposed in Section 3.1, the calculation is performed to obtain the sampling points  $P_2$  and the reference spots for each subaperture on the ideal freeform surface. The sampling points for the central subaperture are shown in Fig. 6(d), and the calculated reference spots are shown in Fig. 6(g) (where the black dots represent the centers of the microlens array, i.e., traditional reference spots). The calculated sampling points for the second concentric subaperture centered at  $(-3.65, 6.32, 0.11)$  are shown in Fig. 6(e), and the calculated reference spots are shown in Fig. 6(h). The sampling points calculated for the center position  $(-10.92, 9.68, 0.40)$  of the third annular aperture are shown in Fig. 6(f), and the calculated reference spot is shown in Fig. 6(i).

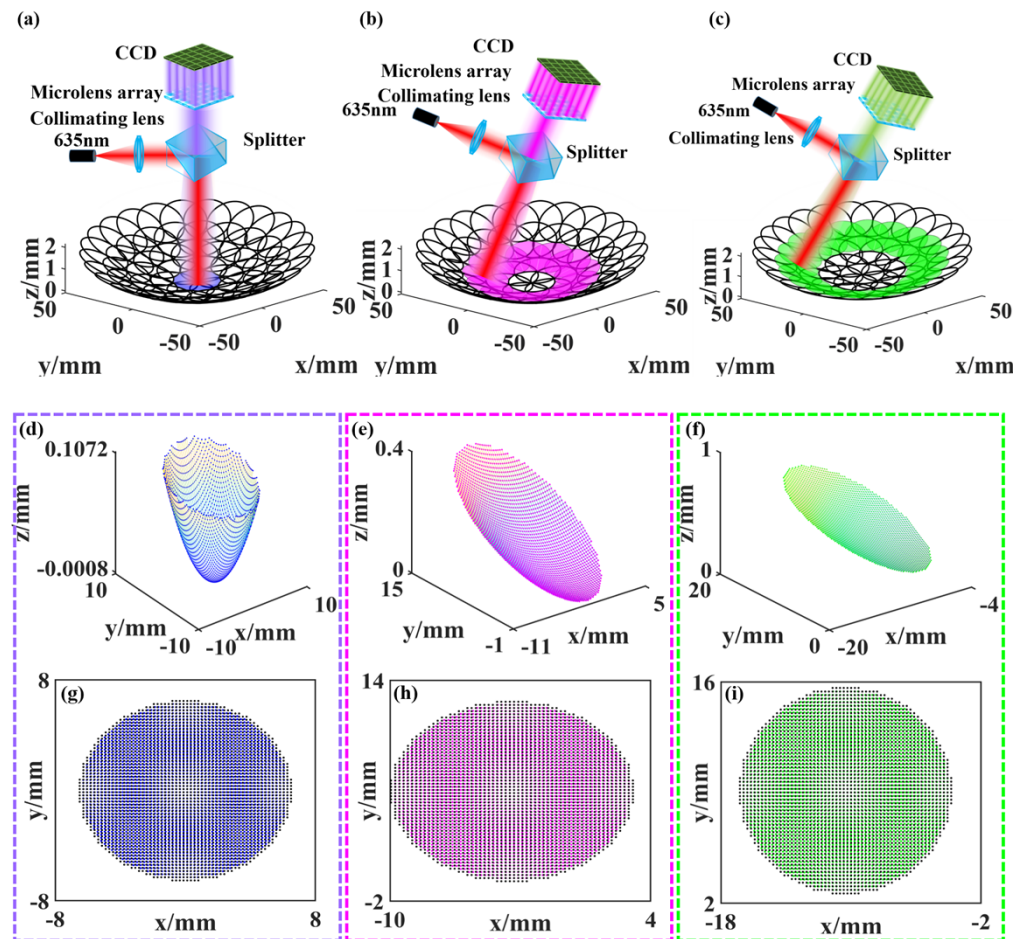


**Fig. 6.** Simulated optical path diagram. (a) Center subaperture simulated optical layout, (b) Second ring subaperture simulated optical layout, (c) Third ring subaperture simulated optical layout. Simulation reference sampling points diagram. (d) Sampling points for center subaperture simulation, (e) Sampling points for second ring subaperture simulation, (f) Sampling points for third ring subaperture simulation. Simulation reference spot map. (g) Center subaperture simulated spot, (h) Second ring subaperture simulated spot, (i) Third ring subaperture simulated spot. Principle verification simulation results.

#### 4.2. Iterative algorithm simulation results

To demonstrate the effectiveness of the proposed iterative method in improving the accuracy of wavefront reconstruction, aberration 1, aberration 2, aberration 3, and aberration 4 with RMS values of  $0.1436 \lambda$ ,  $0.3622 \lambda$ ,  $2.3906 \lambda$ ,  $8.0130 \lambda$  ( $\lambda=635 \text{ nm}$ ) in Fig. 7(a), 7(d), 8(a), and 9(a), respectively, are introduced on top of the ideal freeform surface profile. Firstly, the initial sampling points  $P_2^0$  on the ideal freeform surface are computed based on the established model, which correspond to the simulation result presented in Section 4.1. Secondly, simulations are conducted on the ideal freeform surface by adding aberrations to generate actual spots of light. The slope information is then calculated. The iterative algorithm is utilized to optimize the approximate sampling points  $P_2^n$ , which are subsequently incorporated into the wavefront reconstruction algorithm. Finally, a least squares fitting is performed to obtain the surface form errors. The effectiveness of the iterative method is evaluated by comparing the RMS values of the deviation between the actual sampled points and the approximated sampled points, as well as the RMS values of the input aberrations and the residual errors of the fitted aberration.

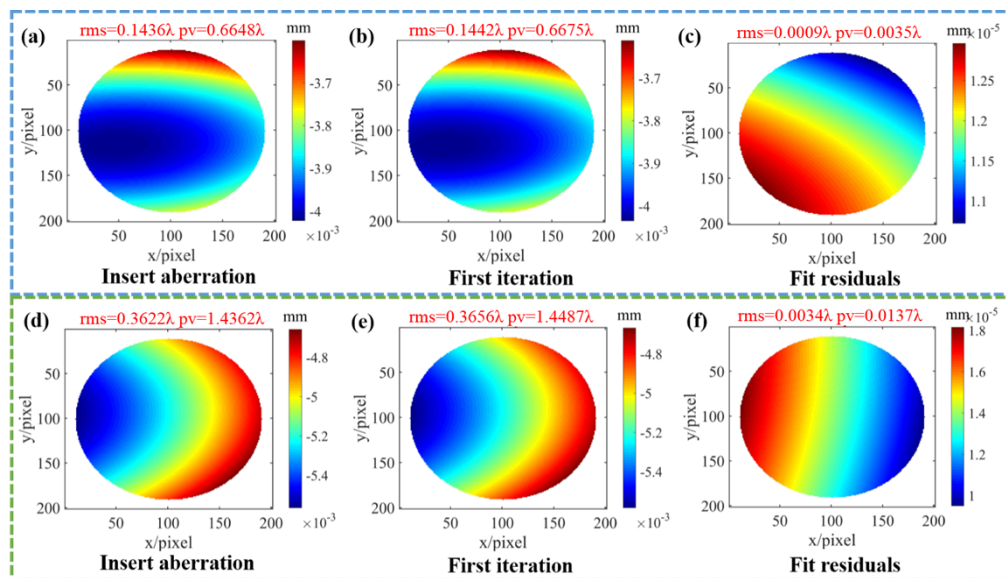


**Fig. 7.** Iterative simulation results with added aberration 1. (a) Wavefront of aberration 1, (b) Fitted full aperture surface error at sampling point  $P_2^0$  using input aberration 1, (c) Residual at sampling point  $P_2^0$  using input aberration 1. Iterative simulation results with added aberration 2. (d) Wavefront of aberration 2, (e) Fitted full aperture surface error at sampling point  $P_2^0$  using input aberration 2, (f) Residual at sampling point  $P_2^0$  using input aberration 2.

The aberration 1 is introduced with an RMS value of  $0.1436 \lambda$  and a PV value of  $0.6648 \lambda$ , as shown in Fig. 7(a). After one iteration, the fitted aberration results in an RMS value of  $0.1442 \lambda$  and a PV value of  $0.6675 \lambda$ , as depicted in Fig. 7(b). The reconstructed wavefront fitting precision is RMS  $0.0009 \lambda$ , as illustrated in Fig. 7(c). The aberration 2 is introduced with an RMS value of  $0.3622 \lambda$  and a PV value of  $1.4362 \lambda$ , as illustrated in Fig. 7(d). After one iteration, the fitted aberration results in an RMS value of  $0.3655 \lambda$  and a PV value of  $1.4487 \lambda$ , as shown in Fig. 7(e). The reconstructed wavefront fitting precision is RMS  $0.0034 \lambda$ , as depicted in Fig. 7(f). The aberration 3 is introduced with an RMS value of  $2.3906 \lambda$  and a PV value of  $10.1355 \lambda$ , as illustrated in Fig. 8(a). After the first iteration (yellow region), the fitted aberration results in an RMS value of  $2.4196 \lambda$  and a PV value of  $10.2637 \lambda$ , as shown in Fig. 8(b). After the second

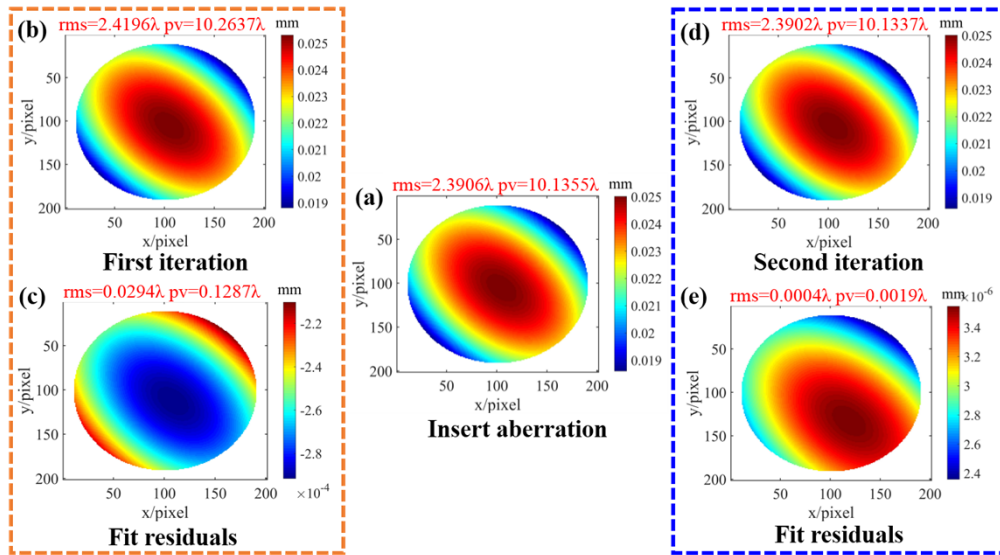


**Fig. 8.** Iterative simulation results with added aberration 3. (a) Wavefront of aberration 3, (b) First iteration fitted full aperture surface error, (c) First iteration residual, (d) Second iteration fitted full aperture surface error, (e) Second iteration residual.

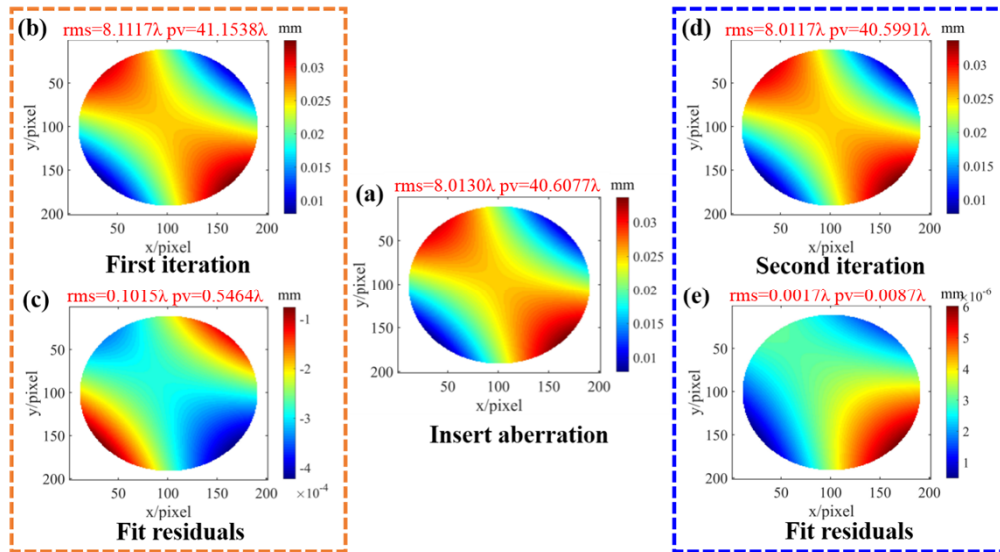


**Fig. 9.** Iterative simulation results with added aberration 4. (a) Wavefront of aberration 4, (b) First iteration fitted full aperture surface error, (c) First iteration residual, (d) Second iteration fitted full aperture surface error, (e) Second iteration residual.

iteration, the fitted aberration results in an RMS value of  $2.3902 \lambda$  and a PV value of  $10.1337 \lambda$ , as depicted in Fig. 8(d). The reconstructed wavefront fitting precision improves from an RMS value of  $0.0294 \lambda$  (Fig. 8(c)) in the first iteration to an RMS value of  $0.0004 \lambda$  (Fig. 8(e)) in the second iteration. The aberration 4 is introduced with an RMS value of  $8.0130 \lambda$  and a PV value of  $40.6077 \lambda$ , as shown in Fig. 9(a). After the first iteration, the fitted aberration results in an RMS value of  $8.1117 \lambda$  and a PV value of  $41.1538 \lambda$ , as illustrated in Fig. 9(b). After the second iteration (blue region), the fitted aberration results in an RMS value of  $8.0117 \lambda$  and a PV value of  $40.5991 \lambda$ , as depicted in Fig. 9(d). The reconstructed wavefront fitting precision improves from an RMS value of  $0.1015 \lambda$  (Fig. 9(c)) in the first iteration to an RMS value of  $0.0017 \lambda$  (Fig. 9(e)) in the second iteration.

Due to the selection of reference sampling point  $P_2^0$  as the initial point in the iterative algorithm, which is close to the actual sampling point  $P_2$ , the wavefront reconstruction accuracy can satisfy the desired requirements with a limited number of iterations. As illustrated in Fig. 10, it can be observed from the line graph that the RMS value of the surface residual error decreases after each iteration, indicating a converging iteration process. The bar chart reveals that the number of iterations required varies for different magnitudes of surface error. It is evident that larger surface errors require a higher number of iterations. This phenomenon can be attributed to the increased deviation between the initial reference sampling point  $P_2^0$  and the actual sampling point  $P_2$ , which compromises the accuracy of the reconstructed wavefront. The red dashed line represents the convergence threshold  $\lambda/100$  ( $\lambda=635 \text{ nm}$ ). The results not only demonstrate the influence of the accuracy of the sampling point coordinates on the precision of wavefront reconstruction but also validate the advantages of the proposed iterative method in improving wavefront reconstruction accuracy.

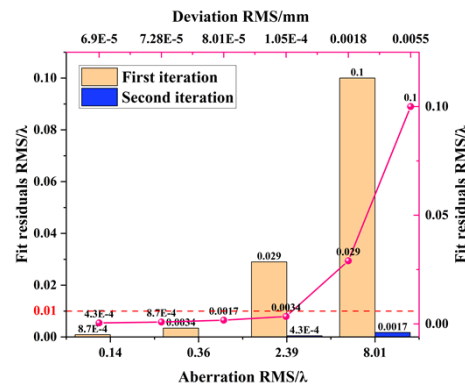


**Fig. 10.** Bar chart: Relationship between input aberration, iteration count, and fitting residual, Line chart: Relationship between deviation of actual sampling points from approximate sampling points and residual of wavefront reconstruction surface.

### 4.3. Precision analysis

To verify the feasibility and robustness of the SHPSS method for testing the error of freeform surface, a simulation experiment is designed to combine the fabrication parameters of freeform surfaces in practical test. The measurement accuracy of the full aperture freeform surface is obtained through error analysis. In practical test, the main sources of errors that affect the measurement accuracy include errors in establishing the system model and related algorithms, positioning errors and angular errors of the scanning mechanism during the testing process, processing and adjustment errors of the measurement system, Shack-Hartmann sensor measurement accuracy, and the influence of environmental factors.

To validate the error of the system model include the inaccurately modeled systems for ray tracing and the computational accuracy of the wavefront fitting algorithms, the reference spots are used as the result of practical test. The slope of the freeform surface is calculated using the reference sampling points according to the method proposed in Section 3.2. As well as the slope difference compares the slope of the ideal freeform surface on the reference sampling points with the slope calculated by the system model in the x and y directions, as shown in Fig. 11(a) and (b) respectively. The wavefront fitting algorithm is used for least squares fitting of the full-aperture surface error, with the result shown in Fig. 11(c). The error of the inaccurately modeled systems for ray tracing and the wavefront fitting algorithm is found to be RMS  $1.95 \times 10^{-10}$  nm, demonstrating the precision of the SHPSS measurement system model. The errors caused by deviations in the positioning system during measurement result in differences between the actual and expected positions, which significantly affect the measurement results. Therefore, random errors in position ( $\pm 0.001$  mm) and angle ( $\pm 1$  second) are introduced into each sub-aperture in the system model within the tolerance range of the scanning mechanism. The influence of pose errors in the scanning mechanism on the full-aperture surface measurement results is analyzed using numerical calculations and statistical methods through Monte Carlo simulation. The simulation results are shown in Fig. 11 (d) to (i) respectively. Due to the excellent manufacturing process and precise calibration, the sensor has very small machining errors. The machining and calibration errors are better than  $\lambda/50$  and can be eliminated through offline calibration methods. The Shack-Hartmann wavefront sensor used in the experiment has a measurement accuracy of  $\lambda/100$  known from the sensor manual. The influence of stray light in the environment mainly consists of mid-to-high frequency errors. The Shack-Hartmann method has a smoothing effect on mid-to-high frequency information and the errors can be suppressed by taking multiple measurements and averaging them. Additionally, the influence of diffraction effects can be neglected by removing the edge data.

In summary, the factors affecting the measurement accuracy of full aperture and the introduced errors in the process of testing freeform surfaces using the SHPSS method are shown in Table 1. Through error synthesis, the measurement accuracy of full-aperture freeform surface is 11.45 nm, demonstrating the feasibility and robustness of the SHPSS method in achieving high-precision surface measurement for freeform surfaces.

**Table 1. The accuracy of the full aperture surface by error factors**

Parameter	Value(RMS nm)
System model and algorithms error	$1.95 \times 10^{-10}$
Position error in x direction	6.81
Position error in y direction	6.56
Position error in z direction	0.17
Attitude error in x direction	0.31
Attitude error in y direction	0.24
Attitude error in z direction	1.08
Shack-Hartmann sensor measurement accuracy	6.35
Measurement accuracy	11.45



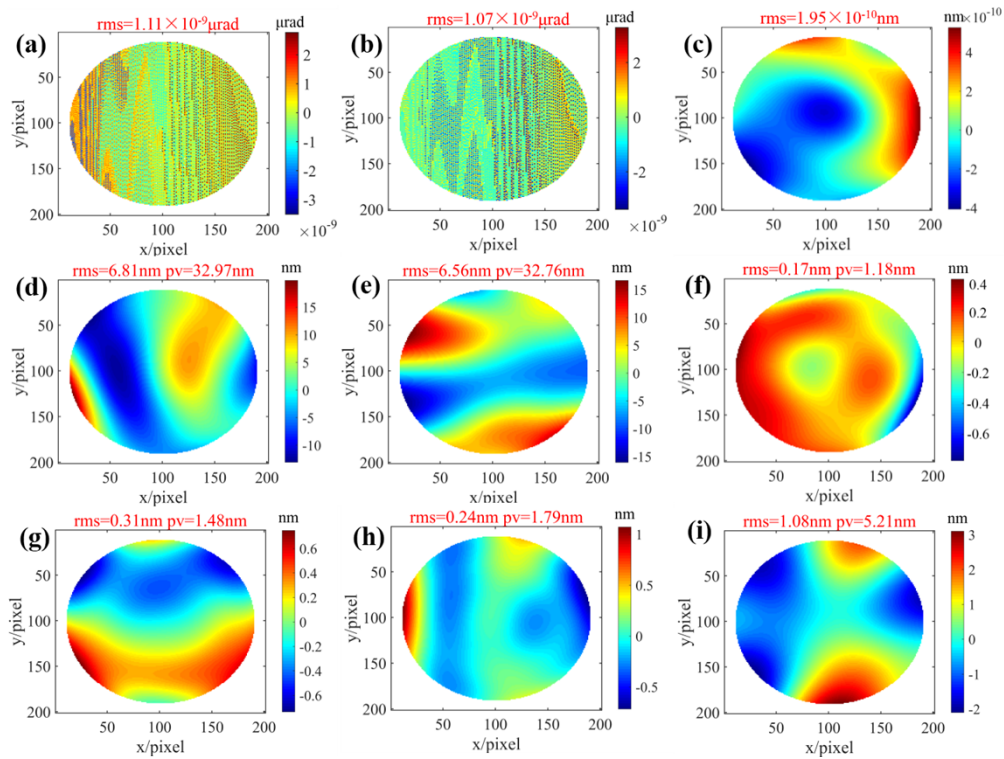


**Fig. 11.** System model error of full aperture. (a) Simulated x direction slope difference for full aperture, (b) Simulated y direction slope difference for full aperture, (c) Simulated surface error for full aperture. Monte Carlo simulation errors of full aperture resulted from the inaccuracy of the scanning mechanism. (d) The full aperture surface error of x direction  $\pm 0.001$  mm random error, (e) The full aperture surface error of y direction  $\pm 0.001$  mm random error, (f) The full aperture surface error of z direction  $\pm 0.001$  mm random error, (g) The full aperture surface error of tilt  $\pm 1$  second random error in x direction, (h) The full aperture surface error of tilt  $\pm 1$  second random error in y direction, (i) The full aperture surface error of rotate  $\pm 1$  second random error in z direction.

## 5. Experimental results

A measurement system is constructed based on the principle diagram in Fig. 1, which enables the scanning of a freeform reflective mirror along the normal direction of the subaperture using small-aperture collimated light emitted by a SHS. The SHS used in the system is the HASO3-128 model manufactured by Imagine Optics, France. It features a microlens array with dimensions of  $128 \times 128$ , with each microlens having an aperture of 0.114 mm and a focal length of 4.1 mm. The accompanying CCD has an effective size of 14.6 mm  $\times$  14.6 mm ( $2048 \times 2048$  pixels), with a pixel size of 7.3  $\mu$ m. The system operates at a wavelength of 0.635  $\mu$ m, and the outgoing beam has a diameter of 14.6 mm. The positioning accuracy of each axis on the translation carrying the system is  $\pm 0.001$  mm. The freeform surface to be tested is the same as that used in the simulation in 4.1. The specific data details is in 4.1, which will not be stated too much here. Due to the suboptimal edge processing of the mirror under test, the actual measuring aperture for the freeform concave mirror is  $D = 100$  mm.

First, the alignment and calibration of the measurement system's collimated light direction are performed using a pinhole aperture stop, as illustrated in Fig. 12(a). When a standard planar mirror is placed at the test position without calibration, the reflected light spot in the CCD is shown

in Fig. 12(b). In this case, the centroid of the light spot (red dot) is located outside the central point (blue circle). The calibration is performed by adjusting the position and orientation of the sensor to ensure that the centroid of the reflected light spot falls within the blue circle. Once calibrated, the centroid of the calibrated light spot changes from red to green, as shown in Fig. 12(c). Next, the pinhole aperture stop is removed, and the measurement system's error is calibrated using the standard planar mirror. Subsequently, the standard planar mirror is replaced with the freeform surface, with a measuring distance of  $d = 10$  mm selected to avoid excessive beam convergence and reduce resolution degradation. The sensor position and tilt angle are adjusted according to the subaperture scheme (as illustrated in Fig. 12(d)) to ensure that the incident direction for each subaperture is along the normal at the center, as depicted in Fig. 14(a). The test for all 133 subapertures is completed sequentially, and the results of some of the subapertures are presented in Fig. 13. In the local subaperture configuration shown in Fig. 13(a), the center subaperture has a center coordinate of (0, 0, 0). The result is illustrated in Fig. 13(b). The result for the first ring of subaperture with the center at (7.300,0,0.101) is shown in Fig. 13(c). The result for the second ring of subaperture with the center at (14.592,0,0.405) is shown in Fig. 13(d). The result for the third ring of subaperture with the center at (21.883,0,0.913) is shown in Fig. 13(e). The result for the fourth ring of subaperture with the center at (29.173,0,1.624) is shown in Fig. 13(e). The result for the fifth ring of subaperture with the center at (36.463,0,2.359) is shown in Fig. 13(g). The result for the sixth ring of subaperture with the center at (43.752,0,3.657) is shown in Fig. 13(h).

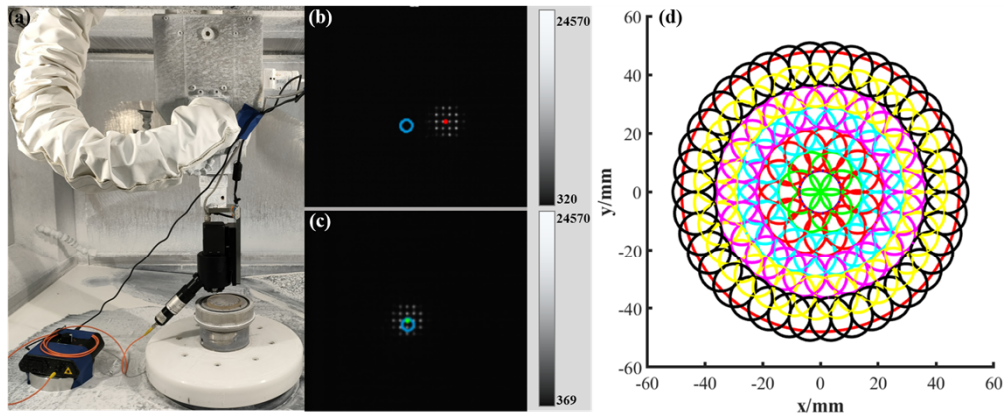


**Fig. 12.** Calibration procedure and subaperture planning result. (a) Calibration of the experimental measurement system, (b) Light spot image when not aligned, (c) Light spot image after calibration, (d) Two-dimensional representation of subaperture program.

The reference spots calculated in Section 3.1 are used to identify and calculate the centroids of the spots on the CCD, which are then matched with the microlens array. The data is processed using both the direct slope method and the iterative method to obtain the full aperture slope deviation. Wavefront reconstruction is performed using the least squares method. The SHPSS experimental results for the full aperture are shown in Fig. 14(c). The RMS is measured to be  $0.043 \lambda$ . To validate the measurement capability of the proposed method, the same freeform reflective mirror is tested using interferometry. The spherical wavefront emitted by the interferometer changes into the wavefront of the vertically incident ideal freeform surface through CGH, and then reflects back to the interferometer. The wavelength of the test light used by the interferometer is 632.8 nm. The device and optical path are illustrated in Fig. 14(b), and the test results are shown in Fig. 14(d). The RMS is measured to be  $0.046 \lambda$  ( $\lambda=632.8$  nm). (Note: The wavelength mentioned in the article, only the unit of the interferometry measurement results is 632.8 nm,

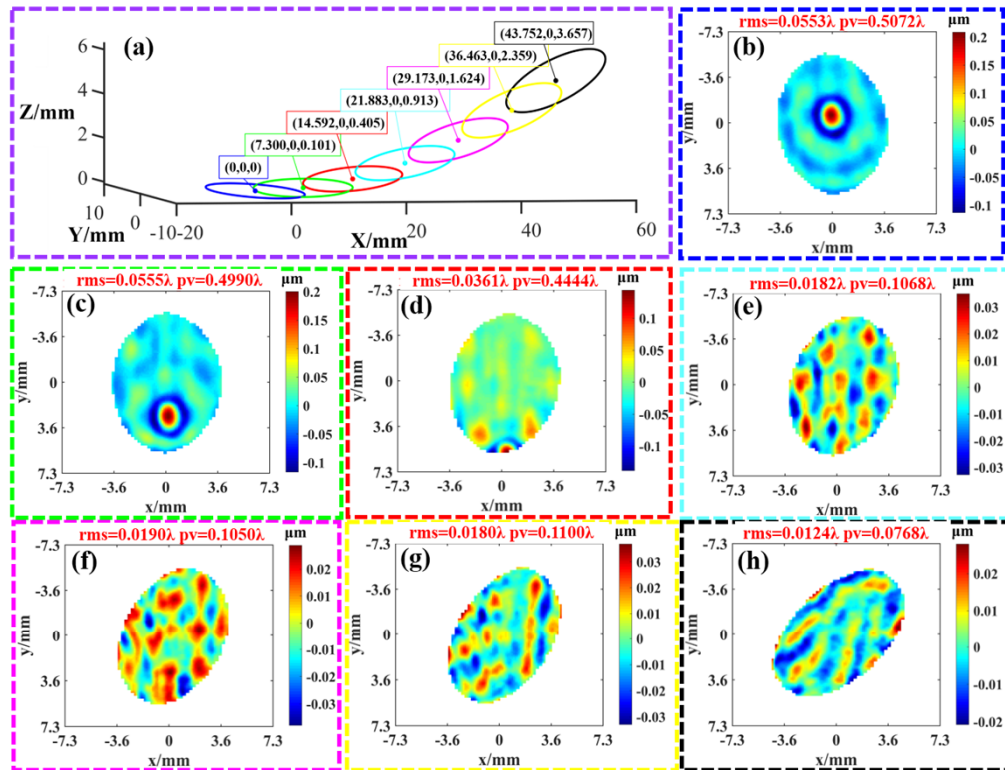


**Fig. 13.** The layout and measurement results of partial subaperture in SHPSS test are presented. (a) Local subaperture planning, (b) Surface error test result with the subaperture centered at (0, 0, 0), (c) Surface error test result with the subaperture centered at (7.300,0,0.101), (d) Surface error test result with the subaperture centered at (14.592,0,0.405), (e) Surface error test result with the subaperture centered at (21.883,0,0.913), (f) Surface error test result with the subaperture centered at (29.173,0,1.624), (g) Surface error test result with the subaperture centered at (36.463,0,2.359), (h) Surface error test result with the subaperture centered at (43.752,0,3.657).

and the rest are 635 nm.) The surface error residual of the two methods has been compared, and the result shows an RMS of  $0.031 \lambda$  as depicted in Fig. 14(e). The residual error is less than the RMS of  $\lambda/30$  that provides evidence for the feasibility of SHPSS in testing the surface error of freeform. This validates its potential as a novel approach for testing freeform surface errors. In addition, the SHS can be combined with the machine tool to measure the freeform surface along the normal direction, so the SHPSS can also achieve on-line measurement during manufacturing.

To verify the stability and reproducibility of the SHPSS method, five sets of repeated testing experiments were conducted. These five sets of testing experiments were carried out consecutively with the same testing parameters. The results of the five testing sets are shown in Fig. 15 respectively. By comparing the wavefront maps of the five testing sets, it is evident that the wavefront profiles of the measurement results are highly consistent, displaying remarkable similarity. The wavefront RMS and PV values are shown in Table 2. The calculated RMS repeatability deviation of the five testing results is  $0.012 \lambda$ , which is less than  $1/80 \lambda$ . This verifies the high repeatability accuracy of the SHPSS method, and further confirms its advantages of stability and resistance to external environmental interference.

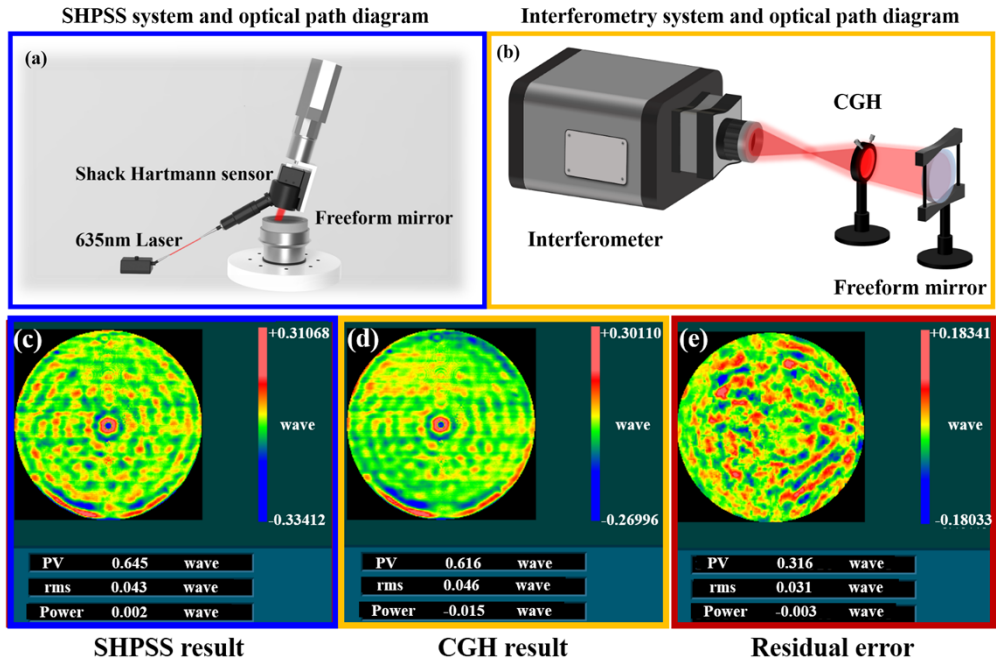


**Fig. 14.** Two methods of measurement system and test results, as well as relative error. (a) SHPSS measurement system, (b) Interferometry system device and optical path, (c) SHPSS test result, (d) Interference test result, (e) Residual error.

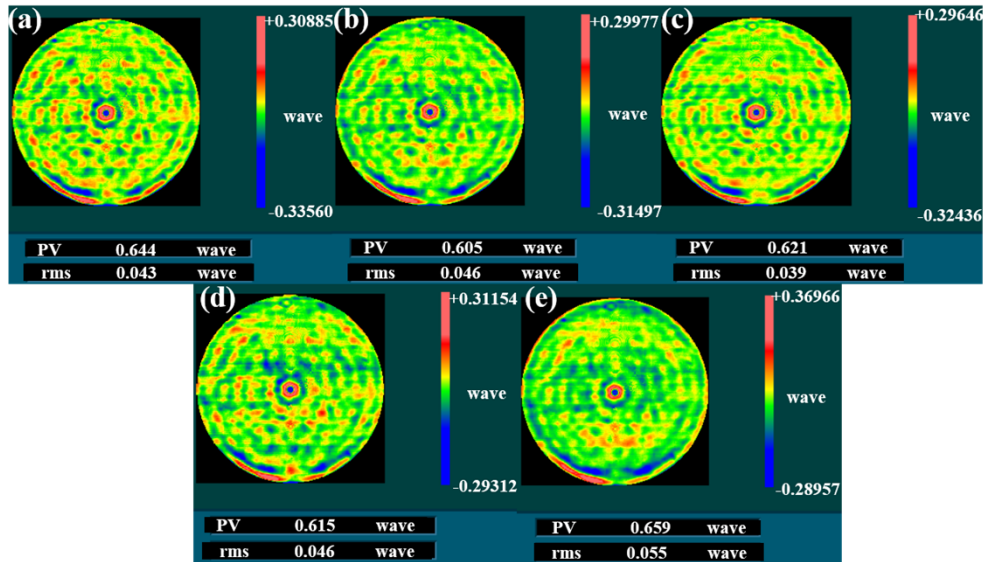


**Fig. 15.** Repetitive testing results of the SHPSS method.

**Table 2. Repetitive test results of RMS and PV for the SHPSS method**

Serial number	RMS( $\lambda$ )	PV( $\lambda$ )
a	0.043	0.644
b	0.046	0.605
c	0.039	0.621
d	0.046	0.615
e	0.055	0.659
Repeatability accuracy(RMS)	0.012	

## 6. Conclusion

In this work, the study proposes a method for testing freeform surfaces using a SHS. This method involves emitting a small aperture collimated beam and scanning it along the normal direction at the center of the sub-aperture to achieve a stitched measurement of the freeform surface. A theoretical mathematical model is established based on ray tracing and the reflection theorem. This model is utilized to calculate the reference sampling points and reference spots, thereby avoiding situations where the spot deviates and cannot be matched with the microlens due to significant system errors. Based on the characteristics of the method, which involves parallel light incidents along the normal direction of the sub-aperture, a direct method for calculating the slopes on the freeform surface is proposed. Through theoretical analysis, it is demonstrated that this method increases the dynamic range of the Shack-Hartmann sensor from 7.1 mrad, as provided by traditional algorithms, to 0.365 rad when the measuring distance is set at 10 mm. Simulation analysis results indicate the feasibility of this method for testing the surface error of freeform surfaces. To improve the accuracy of the reconstructed wavefront, a method for iteratively computing the coordinates of sampling points is proposed. Through numerical simulations, the algorithm achieves an RMS deviation on the order of  $10^{-5}$  mm compared to the true sampling points. When the RMS aberration is 5  $\mu\text{m}$ , the iterative fitting residual can be optimized to 0.0017  $\lambda$ . Through error analysis and synthesis, the measurement accuracy of full-aperture freeform surface is 11.45 nm, demonstrating the feasibility and robustness of the SHPSS method in achieving high-precision surface measurement for freeform surfaces.

An experimental system is established to test a freeform concave reflective mirror with a diameter of 100 mm. The residual of the SHPSS test results (RMS 0.043  $\lambda$ ) and the interference test results (RMS 0.046  $\lambda$ ) is found to be less than the RMS of  $\lambda/30$ . In addition, the method proposed for testing the surface error of freeform surfaces exhibits great versatility. The scanning and stitching method facilitates the test of large-aperture freeform surfaces, while the method employing normal incidence on sub-apertures enables the measurement of freeform surfaces with substantial curvature variations. The SHPSS can also be used for on-line measurement during manufacturing. These findings highlight the broad applicability of the SHPSS method. The repeatability accuracy of the SHPSS method is less than  $1/80 \lambda$  (RMS), and further confirms its advantages of stability and resistance to external environmental interference.

**Funding.** National Natural Science Foundation of China Instrumentation Special Project - High Precision Wide Dynamic Large Aperture Optical Detection System for Fine Astronomy Observation (62127901); Chinese Academy of Sciences National College Students Innovation and Entrepreneurship Training Program (Y9I838S); Foundation of Equipment Pre-research Area[China] (50923020201); Key Basic Research Project of Basic Strengthening Plan (2021-JCQC-ZD-074-12-04); Basic Strengthening Plan Project (2022-JCJQ-JJ-0777).

**Disclosures.** The authors declared that they have no conflicts of interest to this work.

**Data availability.** Data underlying the results presented in this paper are not publicly available at this time but may be obtained from the authors upon reasonable request.

## References

1. X. Zhang, H. Hu, and X. Wang, *et al.*, "Challenges and strategies in high-accuracy manufacturing of the world's largest SiC aspheric mirror," *Light: Sci. Appl.* **11**(1), 310 (2022).
2. J. Reimers, A. Bauer, and K. P. Thompson, *et al.*, "Freeform spectrometer enabling increased compactness," *Light: Sci. Appl.* **6**(7), e17026 (2017).
3. J. P. Rolland, M. A. Davies, and T. J. Suleski, *et al.*, "Freeform optics for imaging," *Optica* **8**(2), 161–176 (2021).
4. M. Elgarisi, V. Frumkin, and O. Luria, *et al.*, "Fabrication of freeform optical components by fluidic shaping," *Optica* **8**(11), 1501–1506 (2021).
5. S. Y. Chen, S. Xue, and D. D. Zhai, *et al.*, "Measurement of Freeform Optical Surfaces: Trade-Off between Accuracy and Dynamic Range," *Laser Photonics Rev.* **14**(5), 1900365 (2020).
6. D. D. Wang, P. Xu, and Z. D. Wu, *et al.*, "Simultaneous multisurface measurement of freeform refractive optics based on computer-aided deflectometry," *Optica* **7**(9), 1056–1064 (2020).
7. C. Y. Zhao, "Computer-Generated Hologram for optical testing - A review," in *Conference on Tribute to James C. Wyant - The Extraordinaire in Optical Metrology and Optics Education*, Proceedings of SPIE (2021).
8. M. Bichra, T. Meinecke, and P. Fesser, *et al.*, "Freeform characterization based on nanostructured diffraction gratings," *Appl. Opt.* **57**(14), 3808–3816 (2018).
9. Y. B. Seo, K. N. Joo, and Y. S. Ghim, *et al.*, "Subaperture stitching wavelength scanning interferometry for 3D surface measurement of complex-shaped optics," *Meas. Sci. Technol.* **32**(4), 045201 (2021).
10. O. Huerta-Carranza, M. Avendano-Alejo, and R. Diaz-Uribe, "Null screens to evaluate the shape of freeform surfaces: progressive addition lenses," *Opt. Express* **29**(17), 27921–27937 (2021).
11. J. DelOlmo-Marquez, G. Castillo-Santiago, and M. Avendano-Alejo, *et al.*, "Ronchi-Hartmann type null screens for testing a plano-freeform surface with a detection plane inside a caustic surface," *Opt. Express* **29**(15), 23300–23314 (2021).
12. H. Y. Lyu, L. B. Kong, and S. X. Wang, *et al.*, "Robust and accurate measurement of optical freeform surfaces with wavefront deformation correction," *Opt. Express* **30**(5), 7831–7844 (2022).
13. V. Akondi and A. Dubra, "Shack-Hartmann wavefront sensor optical dynamic range," *Opt. Express* **29**(6), 8417–8429 (2021).
14. B. R. Swain, C. Dorrer, and J. Qiao, "Telephoto- lens-based Optical Differentiation Wavefront Sensor for freeform metrology," *Opt. Express* **29**(23), 38395–38403 (2021).
15. J. Floriot, X. Levecq, and S. Bucourt, *et al.*, "Surface metrology with a stitching Shack-Hartmann profilometric head," in *Conference on Optical Measurement Systems for Industrial Inspection V*, Proceedings of SPIE (2007).
16. M. Idir, K. Kaznatcheev, and G. Dovillaire, *et al.*, "A 2 D high accuracy slope measuring system based on a Stitching Shack Hartmann Optical Head," *Opt. Express* **22**(3), 2770–2781 (2014).
17. K. K. Pant, D. R. Burada, and M. Bichra, *et al.*, "Subaperture stitching for measurement of freeform wavefront," *Appl. Opt.* **54**(34), 10022–10028 (2015).
18. D. R. Burada, K. K. Pant, and M. Bichra, *et al.*, "Experimental investigations on characterization of freeform wavefront using Shack-Hartmann sensor," *Opt. Eng.* **56**(08), 1 (2017).
19. D. R. Burada, K. K. Pant, and V. Mishra, *et al.*, "Development of metrology for freeform optics in reflection mode," in *Conference on Optical Measurement Systems for Industrial Inspection X part of the SPIE Optical Metrology Symposium*, Proceedings of SPIE (2017).
20. O. Huerta-Carranza, R. Diaz-Uribe, and M. Avendano-Alejo, "Exact equations to measure highly aberrated wavefronts with the Hartmann test," *Opt. Express* **28**(21), 30928–30942 (2020).
21. Y. Li, W. Huang, and S. Chen, *et al.*, "High accuracy wavefront reconstruction with slope and coordinate compensation," in *Conference on Optical Precision Manufacturing, Testing, and Applications / International Symposium on Optoelectronic Technology and Application / Annual Conference of the Chinese-Society-for-Optical-Engineering (CSOE)*, Proceedings of SPIE (2018).
22. M. C. Roggemann, T. J. Schulz, and C. W. Ngai, *et al.*, "Joint processing of Hartmann sensor and conventional image measurements to estimate large aberrations: theory and experimental results," *Appl. Opt.* **38**(11), 2249–2255 (1999).
23. H. Wei, H. Hu, and F. Yan, *et al.*, "Multi-beam array stitching method based on scanning Hartmann for imaging quality evaluation of large space telescopes," *Sci. Rep.* **8**(1), 7272 (2018).
24. M. C. Roggemann and T. J. Schulz, "Algorithm to increase the largest aberration that can be reconstructed from Hartmann sensor measurements," *Appl. Opt.* **37**(20), 4321–4329 (1998).
25. Z. Gao, X. Li, and H. Ye, "Large dynamic range Shack-Hartmann wavefront measurement based on image segmentation and a neighbouring-region search algorithm," *Opt. Commun.* **450**, 190–201 (2019).
26. H. Xu and J. Wu, "Extended-aperture Hartmann wavefront sensor with raster scanning," *Opt. Express* **29**(21), 34229–34242 (2021).

27. D. R. Neal, J. Copland, and D. Neal, "Shack-Hartmann wavefront sensor precision and accuracy," in *Conference on Advanced Characterization Techniques for Optical, Semiconductor, and Data Storage Components*, Proceedings of the Society of Photo-Optical Instrumentation Engineers (Spie) (2002), 148–160.
28. W. H. Southwell, "Wave-front estimation from wave-front slope measurements," *J. Opt. Soc. Am.* **70**(8), 998–1009 (1980).